

Deep Learning Framework for Detecting Ground Deformation in the Built Environment using Satellite InSAR data

Nantheera Anantrasirichai, *Member, IEEE*, Juliet Biggs, Krisztina Kelevitz, Zahra Sadeghi, Tim Wright, James Thompson, Alin Achim, *Senior Member, IEEE* and David Bull, *Fellow, IEEE*

Abstract—The large volumes of Sentinel-1 data produced over Europe are being used to develop pan-national ground motion services. However, simple analysis techniques like thresholding cannot detect and classify complex deformation signals reliably making providing usable information to a broad range of non-expert stakeholders a challenge. Here we explore the applicability of deep learning approaches by adapting a pre-trained convolutional neural network (CNN) to detect deformation in a national-scale velocity field. For our proof-of-concept, we focus on the UK where previously identified deformation is associated with coal-mining, ground water withdrawal, landslides and tunnelling. The sparsity of measurement points and the presence of spike noise make this a challenging application for deep learning networks, which involve calculations of the spatial convolution between images. Moreover, insufficient ground truth data exists to construct a balanced training data set, and the deformation signals are slower and more localised than in previous applications. We propose three enhancement methods to tackle these problems: i) spatial interpolation with modified matrix completion, ii) a synthetic training dataset based on the characteristics of real UK velocity map, and iii) enhanced over-wrapping techniques. Using velocity maps spanning 2015-2019, our framework detects several areas of coal mining subsidence, uplift due to dewatering, slate quarries, landslides and tunnel engineering works. The results demonstrate the potential applicability of the proposed framework to the development of automated ground motion analysis systems.

Index Terms—InSAR, earth observation, ground deformation, machine learning, convolutional neural network, matrix completion.

I. INTRODUCTION

For the last few decades, it has been possible to accurately measure ground deformation from space using Interferometric Synthetic Aperture Radar (InSAR) [1]. Recent advances in processing techniques and computing power (e.g. [2]), coupled with the launch of the Sentinel-1 satellites have laid the foundation for millimetre-scale monitoring of ground deformation across Europe in near real time. This has obvious potential

This work was supported by the Natural Environment Research Council Digital Environment Programme Feasibility Study (NE/S016104/1)

N. Anantrasirichai, A. Achim and D. Bull are with the Visual Information Laboratory, University of Bristol, UK (email: N.Anantrasirichai@bristol.ac.uk, alin.achim@bristol.ac.uk, Dave.Bull@bristol.ac.uk).

J. Biggs is with the School of Earth Sciences, University of Bristol, UK (email: Juliet.Biggs@bristol.ac.uk).

K. Kelevitz, Z. Sadeghi, T. Wright and J. Thompson are with the COMET, School of Earth and Environment, University of Leeds, UK (email: k.kelevitz@leeds.ac.uk, z.sadeghi@leeds.ac.uk, t.j.wright@leeds.ac.uk).

Manuscript received xx, 2020; revised xx, 20xx.

for monitoring ground movement in urban and semi-rural environments. We use the United Kingdom as a test case, where the average annual cost to the insurance industry of ground motion is estimated to be over £250M [3], [4]. Incidents affecting critical infrastructure, such as mainline railways or dams, can be associated with multi-million pound costs, even for a single slope failure event. The sources of deformation are both natural and anthropogenic: subsidence and heave due to the legacy of the coal mining and quarrying industries [5], shrink and swell of shallow clays [6], natural sinkholes [7], landslides [8], coastal erosion [9], and engineering work, such as tunnelling [10].

The Sentinel-1 satellites acquire data over a 250-km swath at a 4 m by 14 m spatial resolution every 6 days on both ascending and descending tracks, generating a large quantity of data. So far, efforts have largely focused on improving data processing methods and capacity [11], but the need for manual inspection and expert interpretation are also barriers to the timely dissemination of information. Various approaches to automatic detection have been tested, for example, the authors in [12] use a threshold of 10mm/yr to identify anomalies in time-series data from Northern Italy. However, applying a threshold in the spatial domain is not reliable due to the effect of reference-point selection and the performance deteriorates heavily for noisy and low coherence signals. Albino et. al. [13] used receiver operating characteristics to demonstrate that applying a cumulative sum control chart [14] to the time-series improves detection performance over simple thresholding. However, both these methods work on individual pixels and do not take into account the high spatial resolution information that is a major advantage for InSAR. Independent Component Analysis (ICA) has been used to separate deformation from noise based on the assumptions that the signals are statistically independent and non-Gaussian [15]–[17]. However, the main drawback for the use of ICA in automated systems is the uncertainty in the order of the separated components, known as the permutation problem [18].

In this paper, we employ a convolutional neural network (CNN) to automatically detect ground deformation across the United Kingdom. The CNN models the spatial characteristics of InSAR data and then recognises the difference between deformation and atmospheric noise. We base our study on a transferable machine learning approach that has already been successfully used for detecting volcanic deformation in global InSAR data [19]–[21]. Adapting these approaches for

detecting urban deformation is conceptually straightforward, but challenging to implement due to the unsuitable nature of available signals for CNN-based algorithms. The sources of deformation in the UK are much shallower and slower than in volcanic environments, meaning the deformation has a smaller magnitude and spatial extent. The spatially variable coherence and associated processing methods means that InSAR data for the UK is typically sparse and has different noise characteristics to volcanic environments.

In this paper, we propose three novel contributions to address these problems: i) spatial interpolation with a modified matrix completion method to tackle sparsity and simultaneously mitigate noise due to atmospheric effects and scatterer properties, ii) a new synthetic dataset for training based on the characteristics of real UK velocity maps, and iii) enhanced over-wrapping techniques with offset and gain to minimise the influence of reference point selection and to increase the likelihood of detecting slow deformation.

II. MATERIALS AND METHODS

A. Convolutional Neural Networks

Convolutional neural networks (CNNs) are a class of deep feed-forward artificial neural networks. They comprise a series of convolutional layers that are designed to take advantage of 2D structures, such as an image. The weights of the filter in each convolutional layer are adjusted during the training process. The low-level features are extracted and connected to more semantic meaning at the deeper layers. In this paper, we want to learn features from the velocity maps that can distinguish deformation from stable ground.

Previous studies have used convolutional neural networks (CNNs) to detect deformation in wrapped InSAR images of volcanic environments [19]–[21]. Wrapped interferograms are used because the high-frequency content of the fringes is easy to identify and provides strong features for the CNN. The work in [19] provided a proof of concept using a test dataset of 30,249 interferograms, compared different pre-trained networks and found AlexNet [22] to be the most effective and used data augmentation to train the network. The subsequent work [20] improved the detection performance by overcoming the lack of positive training data by using synthetic examples, representing deformation, turbulent and stratified atmospheric contributions. Recently, we studied the feasibility of using the CNN to detect slow volcanic deformation by rewrapping cumulative time series [21]. We found that applying a gain of 2 to the interferograms to double the number of fringes can lower the detection threshold by 25–30%, which can be as low as 1.3 cm/year.

In this paper, we use a transfer-learning strategy augmented with fine-tuning the model trained in [20]. Then the CNN model is retrained with some negative samples of the real UK data along with synthetic positive and negative samples, based on the characteristics of the real UK data as described in Section III-B. In the prediction process, the velocity maps are wrapped and converted into a grayscale image (i.e. the pixel values are scaled to $[0, 255]$). Then they are divided into overlapping patches at the required input size for AlexNet

(224×224 pixels). Each patch is then repeatedly shifted (by $28 = 224/8$ pixels in this paper) to cover the entire image. The output of the prediction process is a probability P of there being deformation in each patch. The probabilities from overlapping patches are merged using a rotationally symmetric Gaussian lowpass filter with a size of 20 pixels and standard deviation of 5 pixels.

B. UK InSAR dataset

Fundamentally, all InSAR methods use the phase difference between two radar images to estimate changes in path length between the satellite and the ground surface. However, there are two distinct classes of processing approaches for generating time series of data: small baseline and persistent scatterer (PS). The small baseline technique [23], [24] employs many small distributed scatterers and is commonly used for wide area monitoring, including tectonic and volcanic applications (e.g. <http://comet.nerc.ac.uk/COMET-LiCS-portal/>). It produces a series of 2D images that can be straightforwardly employed by a CNN as shown by [21]. In contrast, permanent or persistent scatterer methods [25], [26] focus on pixels dominated by a stable large reflector. Thus PS methods are well-suited to areas that have strong reflectors, especially man-made objects like buildings and are usually preferred for urban areas [27]. However, the output dataset is sparse and not suitable for input into CNNs, where correlations between adjacent pixels are learnt and used as local features for classification.

The InSAR dataset used in this paper was provided by SatSense Ltd who employ a novel pixel selection method, RapidSAR [2]. This technique works by identifying siblings of the selected pixel, i.e. evaluating nearby pixels with similar phase and amplitude to the selected pixel. This is then used to estimate the coherence of the selected pixel. This avoids the common issue with both persistent scatterer and small baseline methods whereby coherent points may be rejected or incoherent points included, due to the effect of surrounding pixels. The associated information loss and lower SNR is therefore avoided. However, this still corresponds to sparse representation, which is not directly suitable for CNNs.

For the UK-wide study, we use the medium resolution SatSense product (10 m/pixel) for the period of 2015 - 2019 which consists of $66,801 \times 121,501$ pixels. Although time series are available for each point, for this initial proof of concept, we simply use the average velocity for each pixel. In total, there are ~ 64 million velocity measurements on the ascending pass and ~ 29 million on the descending pass. The distribution of measurement locations is uneven with a significantly higher density in urban areas. We also identify three case study areas from the high resolution SatSense product (5 m/pixel). The coal mining area of Normanton and Castleford shows subsidence of more than 2 mm/yr (Fig 5a) and South Derbyshire shows uplift of more than 6 mm/yr (Fig 5d). A linear pattern of subsidence is seen from Battersea Power Station to Kennington in London (Fig 5g). This is the Northern line extension, where two 3.2 km tunnels have been created between 2017-2020. The difference between the

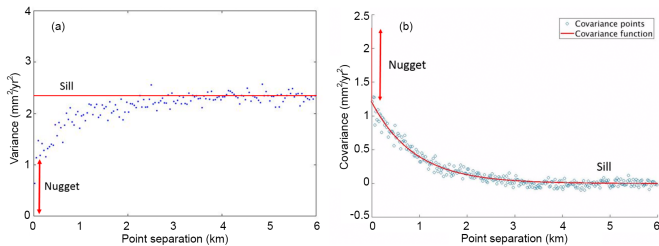


Fig. 1. Spatial characteristics of data in Easton, UK. (a) A 6 km length variogram, showing the nugget near 0, then levels off to a sill of $2.3 \text{ mm}^2/\text{yr}^2$ at point separations of above around 2 km. (b) A covariance function, showing the exponential fitted to the data, the nugget at zero point separation, and the sill as the function levels off at point separations greater than 2 km.

two resolutions is illustrated in Fig. S1 in the supplementary material.

To analyse the spatial characteristics of the SatSense dataset in the UK, we performed a spatial analysis using covariogram [28]. First, a spatial variogram $\gamma(d)$ for point velocity values in space is computed, where d is the distance between the pixels. We found that the variance of point velocity increases sharply (the nugget μ_{nugget}) when the distance between the points is close to zero, then exponentially increases and exhibits a sill μ_{fill} , the background variance value, at long length scales. Consequently, a theoretical variogram is related to a covariance $C(d)$ on the basis of $\gamma(d) = \mu_{sill} - C(d)$. That is, the covariance $C(d)$ decreases exponentially, which is expressed as

$$C(d) = \begin{cases} ae^{-bd}, & \text{if } d > 0 \\ \mu_{sill}, & \text{if } d = 0 \end{cases} \quad (1)$$

where a and b are constants, $a = \mu_{sill} - \mu_{nugget}$, and d is the separation distance in km. From the available UK dataset, we found $a = 0.7 - 1.8 \text{ mm}^2/\text{yr}^2$, $b = 0.8 - 1.6$, and $\mu_{sill} = 1.5 - 2.9 \text{ mm}^2/\text{yr}^2$. This appears as spike noise in the InSAR image and disturbs the gradient calculations performed by the CNN. Thus the spike noise needs to be accounted for when addressing the issue of data sparsity. The plots of the variogram and covariance are shown in Fig. 1.

III. THEORETICAL CONTRIBUTIONS

A. Spatial interpolation

CNNs rely on spatial or sequential attributes of dense data to learn effectively. Adjacent pixels share information that is important and the inherent structure to pixels in image data gives meaning to the overall image. If the data is highly sparse, then the network learns ‘zeros’, the gradient of the loss function is zero and the performance does not improve with iteration. Therefore, it is necessary to interpolate the data during pre-processing to resemble a dense image. Here, we propose and test a novel interpolation method specifically for sparse InSAR data. We illustrate the process using the case study of Normanton and Castleford as shown in Fig. 2 a-c and test the ability of the CNN to identify signals for different types of interpolation in section IV-A.

The simplest way to mathematically describe sparse images is by $y = Mx + n$, where y is the sparse observation of an

ideal dense signal x , M is the sub-sampling matrix, which can be seen as a mask of existing or non existing values, n is noise. Here y is the raw velocity measurements shown in Fig. 2a). This poses an inverse problem for finding x . We employ a matrix completion method (MC) which has been used for compressive sensing [29], where the sparsity of a signal can be exploited to recover it from far fewer samples than required by the Nyquist Shannon sampling theorem [30]. This can be solved with an optimisation process as

$$\hat{x} = \arg \min_x \left\{ \frac{1}{2} \|y - Mx\|_2^2 + \alpha \|x\|_* \right\}, \quad (2)$$

where $\|x\|_*$ is nuclear norm of a matrix (a convex hull of the rank function of x) and α is a regularization parameter. This can be done through a non-convex matrix completion via iterated soft thresholding [31]. The nuclear norm is computed using singular values of matrix x and the process tries to achieve

$$\min_x \|S_x\|_p \text{ subject to } \|y - Mx\|_2 < \varepsilon, \quad (3)$$

where $U_x, S_x, V_x = \text{SVD}(x)$, SVD is singular value decomposition giving the outputs such that $x = U_x S_x V_x'$ and for a non convex function, $0 < p < 1$. The pseudocode to describe this optimisation process is given in Algorithm 1.

First, we generate an initial x_0 by first suppressing some high noise and then applying Delaunay triangulation (DT) (Fig. 2b). To suppress the high-amplitude noise, we simply apply a two-dimensional median filter $\text{Med}_{3 \times 3}(\bullet)$ that omits NaN values in the median calculation. We record the noise map $N = y - \text{Med}_{3 \times 3}(y)$, which will be used later for generating synthetic data with similar characteristics (Section III-B).

In the interpolation process, we add a Gaussian filter $G(x, \sigma)$ with standard deviation σ of 5 pixels, to remove the remaining spike noise in each iteration loop. The proposed technique achieves the estimation of missing pixels and noise reduction simultaneously. Figure 4 shows that the proposed matrix completion method produces more realistic results than conventional Delauney triangulation alone.

B. Synthetic examples

We create 10,000 synthetic datasets (X) for training the CNN using 2 components, namely deformation D , and turbulent atmosphere T , using the simple linear function $X = D + T$. Figure 4 demonstrates the process of synthetic example generation for one example. In this paper, we concentrate on deformation caused by coal mining and tunnelling as they are common in the UK. Therefore we employ two models as follows. i) *A set of synthetic examples of coal mining subsidence*: D_{point} , is generated using a point pressure source model [32], which reproduces the surface deformation associated with inflation and deflation of a subsurface point source. To represent the shallow sources associated with coal mining, we use depths of 3 - 80 m and volume changes of $10^{0.3} - 10^3 \text{ m}^3$. ii) *A set of synthetic examples of tunnelling subsidence*, D_{line} is generated following [33]. The tunnelling-induced subsidence profile is modelled with sagging and

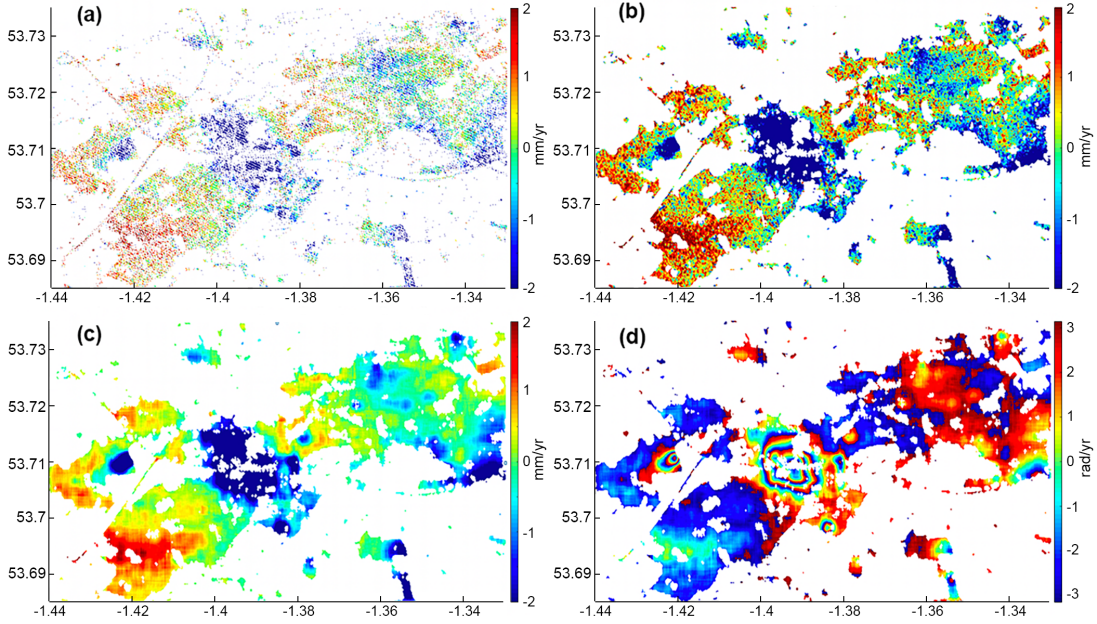


Fig. 2. Velocity map at Normanton and Castleford showing (a) raw sparse data, and its interpolated results from (b) Delauney Triangulation and (c) Matrix Completion techniques. The wrapped velocity map of (c) with the wrap gain $\mu=8$ is shown in (d).

Algorithm 1 Pseudocode of optimization algorithm

Input: $y, x_0, f_0, p, \alpha_0, \alpha, \lambda, \tau, K$

y : sparse observation

x_0 : interpolation using DT and noise suppression

M : sub-sampling matrix

α : regularization parameter, $\alpha_0 = 0.9 \max(|Mx|)$

f : loss, initialised with $f_0 = \|y - Mx_0\|_2 + \alpha_0 \|x_0\|$

p : non-convex norm, $p=0.8$

λ : 1.1-eigenvalue of $(M^{-1}M)$

τ : tolerance, $\tau = 10^{-4}$

C : cost function

K : maximum iterations, $K=200$

Output: $\hat{x} = x$

```

1: while  $\alpha > \tau \alpha_0$  do
2:   for  $k = 1$  to  $K$  do
3:      $x \leftarrow x + \frac{1}{\lambda} M^{-1}(y - Mx)$ 
4:      $U, S, V \leftarrow \text{SVD}(x)$ 
5:      $S \leftarrow \text{diag}\{S\}$ 
6:      $S \leftarrow \text{sign}(S) \max(0, |S| - \frac{1}{2\lambda} \alpha |S|^{p-1})$ 
7:      $x \leftarrow U(\text{diag}\{S\})V'$ 
8:      $x \leftarrow G(x, \sigma)$ 
9:      $f_k \leftarrow \|y - Mx\|_2 + \alpha \|x\|$ 
10:     $C \leftarrow \|f_k - f_{k-1}\| / \|f_k + f_{k-1}\|$ 
11:    if  $C < \tau$  then
12:      break
13:    end if
14:  end for
15:   $\alpha \leftarrow 0.9 \alpha$ 
16: end while

```

hogging zones as demonstrated in Fig. 3a, where the length and depth parameters of sagging and hogging zones are l_{sag} , l_{hog} , d_{sag} and d_{hog} , respectively. We use both l_{sag} and l_{hog} in a range of 30 - 80 m, d_{sag} of 1 - 10 mm, and d_{hog} of 1 - 5 mm. D_{line} is generated by varying these parameters along the curve and straight lines, replicating the track of the underground rail. The 3D displacement vector is then projected to line of sight

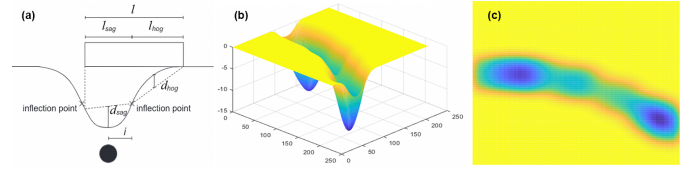


Fig. 3. Synthetic tunnelling subsidence generated following the model introduced in [33], where the cross section profile is shown in (a). Our three-dimensional (3D) synthetic deformation and its projection to create two-dimensional (2D) unwrapped velocity map are shown in (b) and (c), respectively.

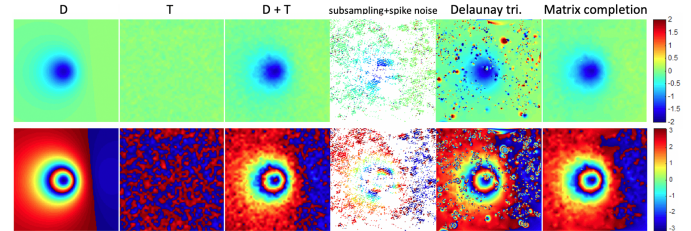


Fig. 4. Synthetic example showing (top row) unwrapped and (bottom row) wrapped samples.

(LOS) using Sentinel-1 UK incidence and heading angles for ascending and descending passes. For both cases, the range of parameters is chosen so that the LOS velocity is in the range 0-15 mm/yr. Note that, in this paper, we trained the models of D_{point} and D_{line} separately, but they could be merged to train a 3-class model (2 types of deformation and non-deformation) in the future.

The satellite measurements of displacement are affected by atmospheric delays caused primarily by water vapour in the troposphere, T . The delays are spatially correlated and their covariance is described in Section II-B. For simplicity, the statistical properties of the atmosphere are assumed to be

radially symmetric and have a homogeneous structure [34]. We use Monte Carlo samples of these distributions to generate synthetic variance-covariance matrices and use a Cholesky decomposition to produce synthetic images with the corresponding statistical properties [20]. For previous applications to volcanic environments, we have also considered a stratified atmospheric component related to the high relief of volcanic edifices. This effect is small in the UK and is neglected here.

We then sub-sample the combined image ($D+T$) using randomly chosen distributions of points from the SatSense data and add spike noise as described in Section II-B. Finally the sparse signals are interpolated as described in Section III-A.

C. Overwrapping and phase shifting

We wrap the velocity map to provide strong features for machine learning [19]. To deal with different deformation rates, we combine a range of wrapping intervals following the method of [21], which was originally designed to detect slow, sustained volcanic deformation in time-series data, but can be adapted for detecting slow, localised motion in the UK velocity measurements. Theoretically, the number of fringes can be increased without altering the signal to noise ratio by reducing the wrap interval (μ). In this paper, following Sentinel-1 line-of-sight where one fringe represents 28 mm of displacement, we employ wrap intervals of 14 mm/yr, 7 mm/yr, 3.5 mm/yr, and 1.75 mm/yr in the prediction process.

One problem with wrapping the velocity map is that different reference points cause the wrap discontinuities to occur in physically arbitrary locations. For some choices of reference points, the number of fringes will increase, but for others it will decrease or for very small signals, fail to produce any discontinuities at all. To ensure that fringes exist on the test image, a constant offset τ is added to the velocity map ψ producing ψ'_τ , i.e. $\psi'_\tau \equiv \psi + \tau \pmod{\mu}$. We run 4 offsets, and select the maximum probability from the CNN for each wrap interval μ , i.e. $P_\mu = \max\{P_{\mu,\tau}\}$, $\tau \in \{0, 3.5, 7, 10.5\}$ mm/yr, and $\mu \in \{14, 7, 3.5, 1.75\}$ mm/yr. The final result is the average of the four probabilities, i.e. $P_{\text{final}} = \frac{1}{4} \sum_{\forall \mu} P_\mu$.

D. Combining different line of sight geometries

One limitation of InSAR technology is that the ground motions are measured in a one-dimensional line of sight (LOS) geometry, whilst the actual surface motions can occur in three dimensions. This means the deformation detected in one LOS direction might not be able to be detected in another LOS direction. However, an advantage is that noise causing a false positive result that appears in one acquisition might not affect the acquisition in another LOS. Therefore in this study, if the areas have both ascending and descending passes available, the two velocity maps are processed independently and the final probability results are obtained from the average. If there are four looks (2 ascending and 2 descending passes), the final probability map will be the maximum of four averages between a pair of ascending and descending signals.

TABLE I
CLASSIFICATION PERFORMANCES (%) WHEN TRAINING WITH SPARSE
AND INTERPOLATED EXAMPLES

| Dataset | Accuracy | Precision | Recall | False positive rate |
|------------|----------|-----------|--------|---------------------|
| Sparse | 54.32 | 63.91 | 53.62 | 55.27 |
| Interp. DT | 89.06 | 99.10 | 82.52 | 20.98 |
| Interp. MC | 98.58 | 99.27 | 97.93 | 2.09 |

IV. RESULTS AND DISCUSSION

A. Spatial interpolation

We first investigate the performance of the proposed spatial interpolation technique using synthetic datasets. Three approaches are tested i) sparse examples without interpolation, ii) interpolated examples with Delauney Triangulation (DT), and iii) interpolated examples using the proposed Matrix Completion (MC) approach (see Fig. 4 last three columns). The CNNs are trained with two classes: $D + T$ (positive) and T (negative). Each class contains 10,000 synthetic samples. When training the CNN with sparse examples, the results of convolution processes are computed from the pixels that have values only. The classification results are shown in Table I. It is obvious that without spatial interpolation, the CNN cannot distinguish between deformation and non-deformation (the accuracy is around 50%). The CNN performs significantly better with dense datasets with an improvement of accuracy by 64.0% with the initial DT and 81.5% with the proposed MC. The DT produces 10 times more false positives than the MC due to spike noise (the nugget - see Section II-B).

B. Application to case study sites

Initially, we test our machine learning algorithms on well-known case study examples of coalfield subsidence D_{point} and tunnelling D_{line} (as described in Section III-B) using the high resolution InSAR product (5 m/pixel). The models are trained separately, using the synthetic examples. The detection results are shown in Fig. 5, where the first, the second and the third columns show i) raw InSAR data, ii) wrapped and interpolated velocity maps used as inputs of the CNNs, and iii) the probability values overlaid on the velocity maps, respectively. The first and the second rows are the results from the coalfields at Normanton and Castleford, and South Derbyshire, detected with the model D_{point} . The velocity map at South Derbyshire has fewer data points causing more difficulties for the interpolation step than that at Normanton and Castleford, but the detection algorithm still works well in both cases. The last row of Fig. 5 shows the detected tunnelling subsidence in London using the model D_{line} . Interestingly the model detects the line of the tunnel but do not pick out the point-source deformation (on the right of the image). These case study results are promising and warrant further testing to check the generalisation of the model and the applicability to a larger scale map.

C. Whole UK velocity map

As described in Section II-B, there are ~ 64 million points of sparse UK data. This is equivalent to a 2D image with

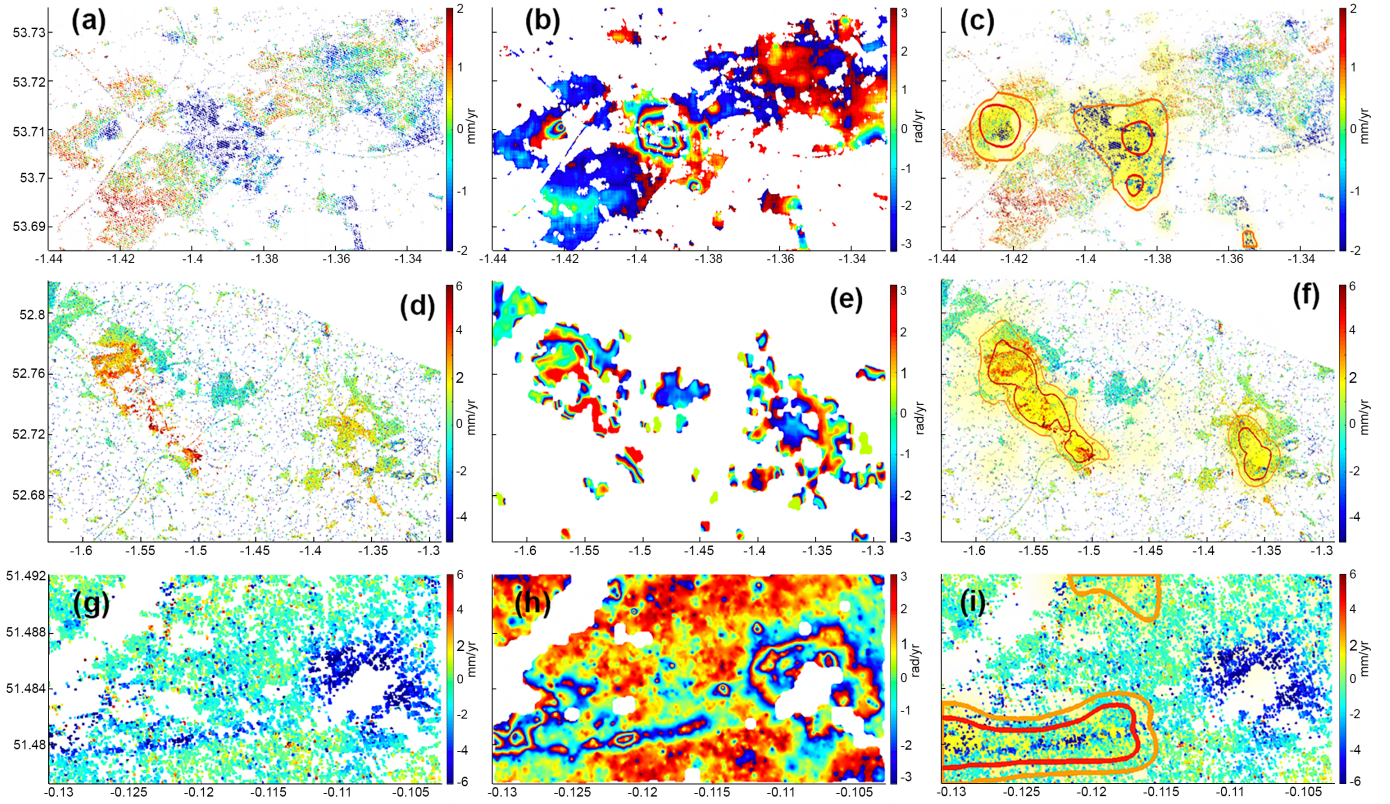


Fig. 5. Detection results in (a-c) Normanton and Castleford, (d-e) South Derbyshire, and (g-i) London – Northern line extension. (a), (d) and (g) are raw data. (b), (e) and (h) are the wrapped and interpolated velocity maps. (c), (f) and (i) are probability maps overlaid on the raw data. The brighter yellow means higher probability. Areas inside orange and red contours are where $P > 0.5$ and $P > 0.75$, respectively.

a resolution of $98,504 \times 68,504$ pixels, which is more than 3,250 full HD TVs combined. To automatically process this large velocity map, we divide it into several 2500×2500 maps, defined by the limitation of memory required to process the spatial interpolation. After spatially interpolating, each velocity map is further divided into overlapping patches following the detection process described in Section II-A. The detected deforming locations using model D_{point} and D_{line} are plotted in Fig. 6 and Fig. 7, showing three levels of probability P , which are >0.5 , >0.75 and >0.9 . In the supplementary material (Fig. S2 and S3) we show areas with detection probabilities >0.5 in more detail.

Fig. 6 shows the results of the D_{point} model. The method detects numerous deforming areas in well-known coal-mining regions from the Midlands up towards Leeds (area A in Fig 6), in South Wales (area B [35]), Normanton and Castleford (area C), North Staffordshire in Stoke-on-Trent (area D [36]), North-west Leicester (area E [37]), Northumberland and Durham (area F [38]). Several areas are detected in London, where recent engineering work has taken place. For example, the detected uplift at Canning Town, London, could be affected by groundwater rebound after completion of dewatering works for the underground construction (area G [39]). In the northwest of Wales, the method detects subsidence from some former slate quarries (area I), including the Dinorwic Quarry near Llanberis (Fig. 6c), the Penrhyn Quarry near Bethesda, and the Ffestiniog Slate Quarry in Blaenau Ffestiniog, where the

slate was mined rather than quarried. The method also detects subsidence of clay works in Kingsteignton (area J, Fig. 6d). Uplift was detected at Golborne, Leigh and Manchester (area K) with a similar spatial extent to the subsidence reported between 1992–2000 [40].

Although we are dominantly considering vertical deformation, horizontal motion associated with landslides and coastal processes will also cause displacements in the line of sight (see Fig. S4 in the supplementary material). For example, landslides with significant horizontal motion were detected south of Kirkby Stephen (area H [41]).

Fig. 7 shows the results of the D_{line} model. We did not include examples of uplift in either positive or negative training datasets for D_{line} , but nonetheless, we detect several uplifting features because the fringes in the wrapped velocity map have characteristics closer to the positive samples than the negative ones. Since uplift and subsidence can be simply distinguished by comparing the velocity with that of neighbouring areas, this information can be added in post-processing. The only detection of tunnelling subsidence in London was at the case study site shown in Fig. 5g-5i, but there were several detections elsewhere in the UK, particularly in the Midlands. Several of these are elongated areas of subsidence more in keeping with mining (for example following coal seams) than infrastructure tunnels (Area A in Fig. 7). In several cases, linear features are associated with linear surface structures, such as roads, probably due to the higher density of measurement points

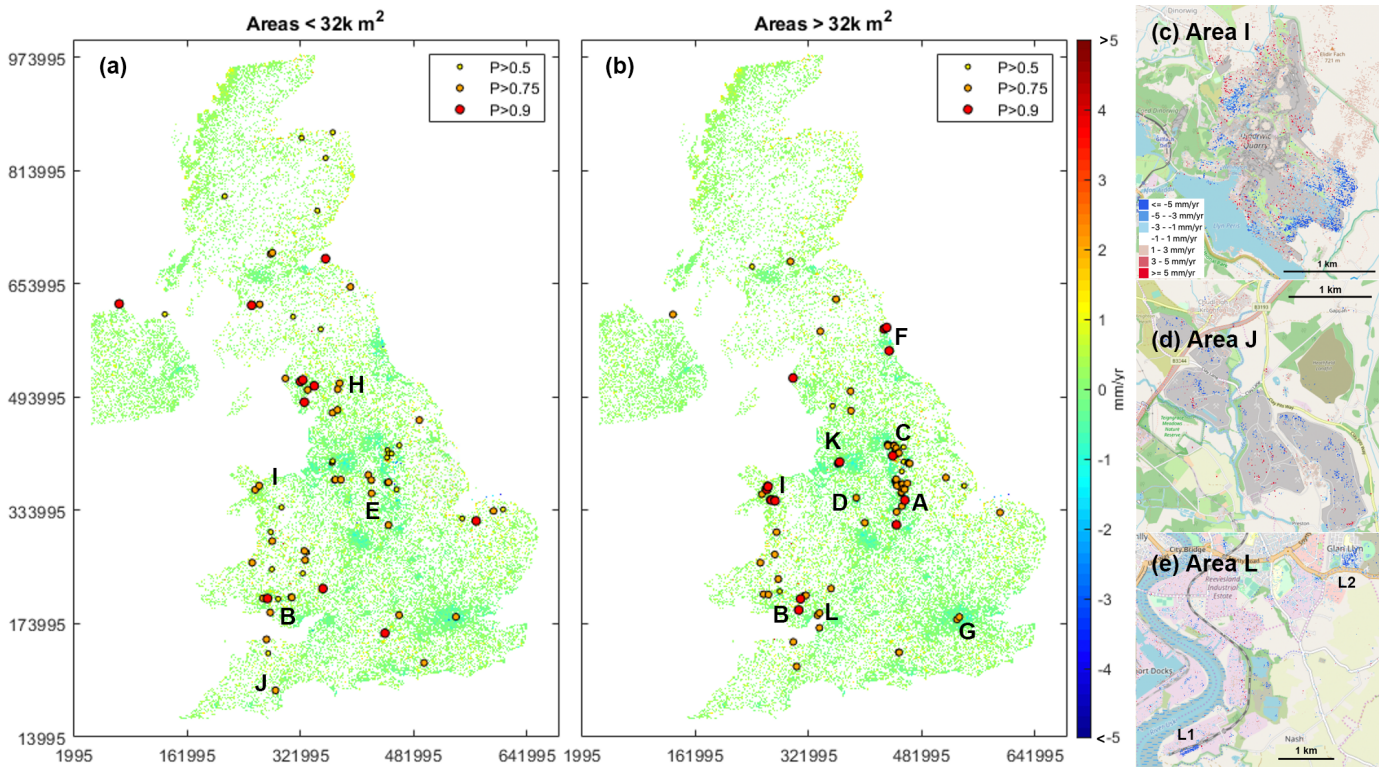


Fig. 6. Detection results in the 10-m velocity map showing the centre locations where the CNN using D_{point} identifies with high probability of being deformation. For visualisation, the small and large areas are plotted separately: (a) the area size less than 32 km², and (b) the area size larger than 32 km². Right column shows ground subsidence due to anthropogenic sources at (c) the Dinorwic quarry in North Wales (Area I), (d) the clay works in Kingsteignton (Area J), (e) the coal yard of Uskmouth power station (L1) and residential areas around Brinell Square (L2) in Newport (Area L).

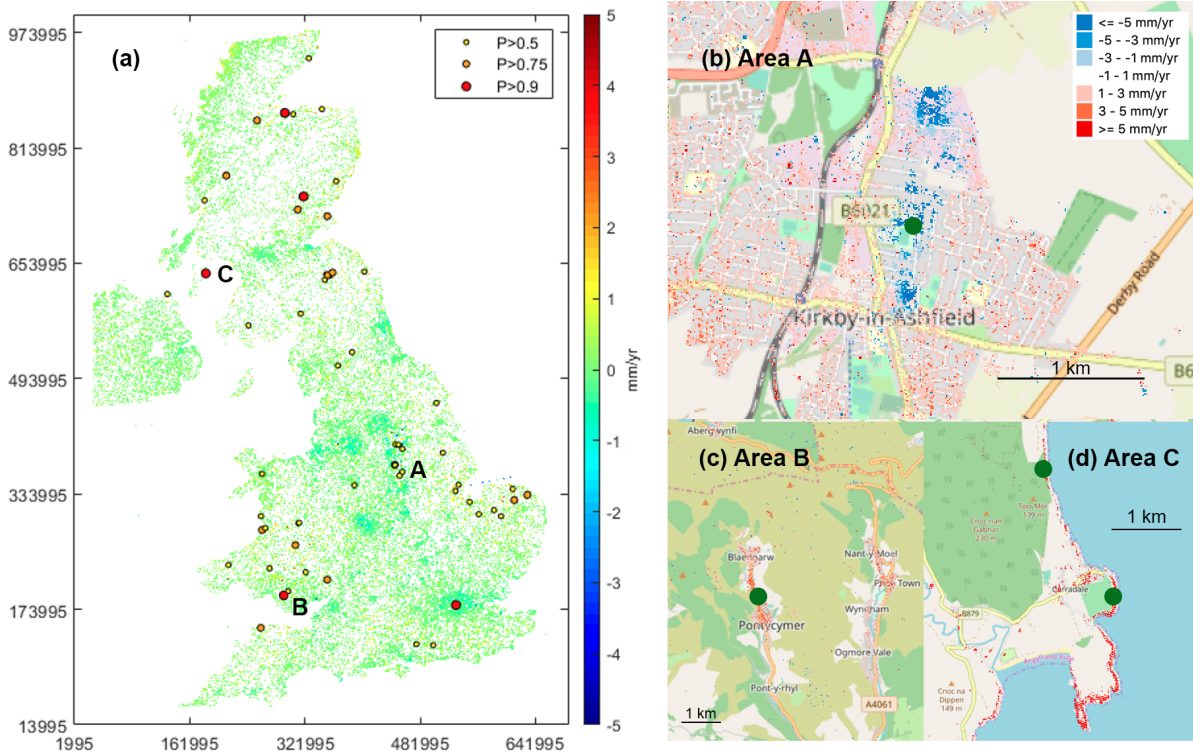


Fig. 7. Detection results in the 10-m velocity map (a) showing the centre locations where the CNN using D_{line} identifies with high probability of being deformation. Examples of linear deformation in (b) Kirkby-in-Ashfield (Area A), (c) Pontycymer, Wales (Area B), (d) uplift coastline in Carradale, Scotland (Area C). The green dots on (b)-(d) are the centre of detected areas.

on the man-made structures than in the surrounding fields. The deformation signal itself is unlikely to be linear, but this enables us to identify deformation sources that might be missed by the d_{point} model due to the uneven sampling of data (e.g. Fig. 7c). In several places, rocky foreshores are picked out, such as the coastline in Carradale (Fig. 7d), which appears to be uplifting relative to the nearest inland point. We attribute this to processing artefacts within the InSAR data.

D. Discussion

Monitoring ground deformation is crucial in urban and semi-urban areas. The UK has a long history of coal mining, and associated water pumping causes surface deformation which can extend to city-sized regional areas. Slope instability can lead to localised damage both in hilly areas and coastal regions. Ground motion can have negative impacts on infrastructure, particularly long linear assets such as drainage networks and pipelines. An example of the need of ground movement detection is for the proposed HS2 route for high speed rail¹ from Birmingham to Leeds, which would pass through the large coalfield areas in Nottingham and Sheffield. Fig. 6 and Fig. 7 show clear ground deformation in these areas and although the velocity rate is only millimetres per year, it still needs to be factored into construction plans.

This paper is a proof-of-concept that demonstrates the potential applicability of the deep learning framework to the development of automated ground motion analysis for anthropogenic sources of deformation in urban and semi-urban environments. We test the deep learning framework on the UK dataset and produce a probability map of surface movement. As the dataset is very large (see Section IV), it would not be feasible to manually inspect the entire area at high resolution. Using a probability threshold of 0.5, the method produces some false positives and false negatives. However, the probability values and the sizes of the detected areas can be employed to prioritise further analysis.

This approach is not restricted to the UK dataset and could be used for any national or regional velocity map, including the European Ground Motion Service currently proposed by Copernicus [42]. The main limitation of the current framework is that it cannot detect very localised deformation, like sinkholes, because their spatial characteristics are too similar to noise. These areas however show clear changes in the time domain. Future developments can incorporate both time-series analysis and spatio-temporal (3D) analysis of InSAR data. Moreover, if both ascending and descending passes are available for the same period of time, 4D signals can be used. In this paper, we train the model using only one pass (2D), and the results of both passes are averaged (Section III-D). If both passes are concatenated and trained together, we expect that the deformation signals would be shown in both passes, so the number of false positives arising from using only one pass will be diminished.

¹<https://www.hs2.org.uk>

V. CONCLUSIONS

This paper demonstrates the feasibility of using a transferable CNN approach to detect ground deformation in urban and semi-urban areas in the UK. We analyse characteristics of the data and propose several adaptations to previously developed deep learning methods. Matrix completion is used to overcome the sparse and uneven measurement distribution and simultaneously reduce spike noise. Synthetic examples based on point sources and tunnels are used for training due to lack of real signals of deformation. Finally overwrapping and phase shifting techniques are employed to enhance features and hence reduce the detection threshold. The methods are tested using the velocity map generated by SatSense Ltd. dated between 2015-2019 and successfully detect several types of deformation occurring around the UK.

ACKNOWLEDGMENT

The authors would like to thank SatSense Ltd. for providing UK datasets.

REFERENCES

- [1] D. Massonnet and K. L. Feigl, "Radar interferometry and its application to changes in the earth's surface," *Reviews of Geophysics*, vol. 36, no. 4, pp. 441–500, 1998.
- [2] K. Spaans and A. Hooper, "InSAR processing for volcano monitoring and other near real time applications," *Journal of Geophysical Research Solid Earth*, vol. 121, pp. 2947–2960, 2016.
- [3] S. Plante, M. MacQueen *et al.*, "A review of current research relating to domestic building subsidence in the uk: what price tree retention?" *A review of current research relating to domestic building subsidence in the UK: what price tree retention?*, no. 017, pp. 219–227, 2012.
- [4] O. G. Pritchard, S. H. Hallett, and T. S. Farewell, "Soil movement in the uk—impacts on critical infrastructure," *Infrastructure Transitions Research Consortium, Cranfield University, Cranfield*, 2013.
- [5] A. T. McCay, M. Valyrakis, and P. L. Younger, "A meta-analysis of coal mining induced subsidence data and implications for their use in the carbon industry," *International Journal of Coal Geology*, vol. 192, pp. 91–101, 2018.
- [6] D. Aldiss, H. Burke, B. Chacksfield, R. Bingley, N. Teferle, S. Williams, D. Blackman, R. Burren, and N. Press, "Geological interpretation of current subsidence and uplift in the london area, uk, as shown by high precision satellite-based surveying," *Proceedings of the Geologists' Association*, vol. 125, no. 1, pp. 1 – 13, 2014.
- [7] F. Gutiérrez, A. Cooper, and K. Johnson, "Identification, prediction, and mitigation of sinkhole hazards in evaporite karst areas," *Environ Geol*, vol. 53, pp. 1007–1022, 2008.
- [8] J. Chambers, P. Wilkinson, O. Kuras, J. Ford, D. Gunn, P. Meldrum, C. Pennington, A. Weller, P. Hobbs, and R. Ogilvy, "Three-dimensional geophysical anatomy of an active landslide in lias group mudrocks, cleveland basin, uk," *Geomorphology*, vol. 125, no. 4, pp. 472 – 484, 2011.
- [9] J. S. Whiteley, J. E. Chambers, S. Uhlemann, P. B. Wilkinson, and J. M. Kendall, "Geophysical monitoring of moisture-induced landslides: A review," *Reviews of Geophysics*, vol. 57, no. 1, pp. 106–145, 2019.
- [10] P. Milillo, G. Giardino, M. J. DeJong, D. Perissin, and G. Milillo, "Multi-temporal InSAR structural damage assessment: The London crossrail case study," *Remote Sensing*, vol. 10, no. 2, 2018.
- [11] P. González, R. Walters, E. Hatton, K. Spaans, A. McDougall, A. Hooper, and T. Wright, "LicSar: Tools for automated generation of sentinel-1 frame interferograms," *AGU Fall Meeting*, 2016.
- [12] F. Raspini, S. Bianchini, A. Ciampalini, M. D. Soldato, L. Solari, F. Novali, S. D. Conte, A. Rucci, A. Ferretti, and N. Casagli, "Continuous, semi-automatic monitoring of ground deformation using sentinel-1 satellites," *Scientific Reports*, vol. 8, no. 7253, 2018.
- [13] F. Albino, J. Biggs, C. Yu, and Z. Li, "Automated methods for detecting volcanic deformation using sentinel-1 insar time series illustrated by the 2017–2018 unrest at agung, indonesia," *Journal of Geophysical Research: Solid Earth*, vol. 125, no. 2, p. e2019JB017908, 2020.

- [14] E. S. PAGE, "CONTINUOUS INSPECTION SCHEMES," *Biometrika*, vol. 41, no. 1-2, pp. 100–115, 06 1954.
- [15] S. Ebmeier, "Application of independent component analysis to multi-temporal insar data with volcanic case studies," *Journal of Geophysical Research: Solid Earth*, vol. 121, no. 12, pp. 8970–8986, 2016.
- [16] E. Chaussard, P. Milillo, R. Bürgmann, D. Perissin, E. J. Fielding, and B. Baker, "Remote sensing of ground deformation for monitoring groundwater management practices: Application to the santa clara valley during the 2012–2015 california drought," *Journal of Geophysical Research: Solid Earth*, vol. 122, no. 10, pp. 8566–8582, 2017.
- [17] M. E. Gaddes, A. Hooper, M. Bagnardi, H. Inman, and F. Albino, "Blind signal separation methods for insar: The potential to automatically detect and monitor signals of volcanic deformation," *Journal of Geophysical Research: Solid Earth*, vol. 123, no. 11, pp. 10,226–10,251, 2018.
- [18] H. Sawada, R. Mukai, S. Araki, and S. Makino, "A robust and precise method for solving the permutation problem of frequency-domain blind source separation," *IEEE Transactions on Speech and Audio Processing*, vol. 12, no. 5, pp. 530–538, Sep. 2004.
- [19] N. Anantrasirichai, J. Biggs, F. Albino, P. Hill, and D. Bull, "Application of machine learning to classification of volcanic deformation in routinely-generated inSAR data," *Journal of Geophysical Research: Solid Earth*, vol. 123, no. 8, pp. 6592–6606, August 2018.
- [20] N. Anantrasirichai, J. Biggs, F. Albino, and D. Bull, "A deep learning approach to detecting volcano deformation from satellite imagery using synthetic datasets," *Remote Sensing of Environment*, vol. 230, p. 111179, 2019.
- [21] —, "The application of convolutional neural networks to detect slow, sustained deformation in insar time series," *Geophysical Research Letters*, 2019.
- [22] A. Krizhevsky, I. Sutskever, and G. E. Hinton, "Imagenet classification with deep convolutional neural networks," in *Proceedings of the 25th International Conference on Neural Information Processing Systems*, vol. 1, 2012, pp. 1097–1105.
- [23] P. Berardino, G. Fornaro, R. Lanari, and E. Sansosti, "A new algorithm for surface deformation monitoring based on small baseline differential sar interferograms," *IEEE Transactions on Geoscience and Remote Sensing*, vol. 40, no. 11, pp. 2375–2383, 2002.
- [24] D. A. Schmidt and R. Bürgmann, "Time-dependent land uplift and subsidence in the santa clara valley, california, from a large interferometric synthetic aperture radar data set," *Journal of Geophysical Research: Solid Earth*, vol. 108, no. B9, 2003.
- [25] A. Hooper, H. Zebker, P. Segall, and B. Kampes, "A new method for measuring deformation on volcanoes and other natural terrains using insar persistent scatterers," *Geophysical Research Letters*, vol. 31, no. 23, 2004.
- [26] M. Crosetto, O. Monserrat, M. Cuevas-González, N. Devanthéry, and B. Crippa, "Persistent scatterer interferometry: A review," *ISPRS Journal of Photogrammetry and Remote Sensing*, vol. 115, pp. 78 – 89, 2016, theme issue 'State-of-the-art in photogrammetry, remote sensing and spatial information science'.
- [27] T. Lauknes, J. Dehls, Y. Larsen, K. Høgda, and D. Weydahl, "A comparison of SBAS and PS ERS InSAR for subsidence monitoring in Oslo, Norway," *Fringe Workshop; European Space Agency*, p. 58, 2005.
- [28] H. Wackernagel, *Multivariate Geostatistics: An Introduction with Applications*. Springer, 2003.
- [29] D. Yang, G. Liao, S. Zhu, X. Yang, and X. Zhang, "Sar imaging with undersampled data via matrix completion," *IEEE Geoscience and Remote Sensing Letters*, vol. 11, no. 9, pp. 1539–1543, Sep. 2014.
- [30] E. J. Candes and Y. Plan, "Matrix completion with noise," *Proceedings of the IEEE*, vol. 98, no. 6, pp. 925–936, June 2010.
- [31] J. Cai, E. J. Candés, and Z. Shen, "A singular value thresholding algorithm for matrix completion," *SIAM Journal on Optimization*, vol. 20, no. 4, pp. 1956–1982, 2010.
- [32] K. Mogi, "Relation between the eruptions of various volcanoes and deformations of the ground surfaces around them," *Bull. Earthquake Res.*, vol. 36, pp. 99–134, 1958.
- [33] G. Giardina, P. Milillo, M. J. DeJong, D. Perissin, and G. Milillo, "Evaluation of InSAR monitoring data for post tunnelling settlement damage assessment," *Structural Control and Health Monitoring*, vol. 26, no. 2, 2018.
- [34] B. Parsons, T. Wright, P. Rowe, J. Andrews, J. Jackson, and R. Walker, "The 1994 sefiadbeh (eastern iran) earthquakes revisited: new evidence from satellite radar interferometry and carbonate dating about the growth of an active fold above a blind thrust fault," *Geophys. J. Int.*, vol. 164, no. 1, pp. 202–217, 2006.
- [35] L. Bateson, F. Cigna, D. Boon, and A. Sowter, "The application of the intermittent sbas (isbas) insar method to the south wales coalfield, uk," *International Journal of Applied Earth Observation and Geoinformation*, vol. 34, pp. 249 – 257, 2015.
- [36] M. Culshaw, L. Tragheim, D. and Bateson, and L. Donnelly, "Measurement of ground movements in Stoke-on-trent (UK) using radar interferometry," in *10th Congress of the International Association for Engineering Geology and the Environment, Nottingham*, vol. 6.
- [37] A. Sowter, L. Bateson, P. Strange, K. Ambrose, and M. F. Syafiudin, "DInSAR estimation of land motion using intermittent coherence with application to the south derbyshire and leicestershire coalfields," *Remote Sensing Letters*, vol. 4, no. 10, 2013.
- [38] D. Gee, L. Bateson, A. Sowter, S. Grebby, A. Novellino, F. Cigna, S. Marsh, C. Banton, and L. Wyatt, "Ground motion in areas of abandoned mining: Application of the intermittent SBAS (ISBAS) to the Northumberland and Durham coalfield," *Geosciences*, vol. 7, no. 2, 2017.
- [39] R. Boní, A. Bosino, C. Meisina, A. Novellino, L. Bateson, and H. McCormack, "A methodology to detect and characterize uplift phenomena in urban areas using sentinel-1 data," *Remote Sensing*, vol. 10, no. 4, 2018.
- [40] F. Cigna and A. Sowter, "The relationship between intermittent coherence and precision of isbas insar ground motion velocities: Ers-1/2 case studies in the uk," *Remote Sensing of Environment*, vol. 202, pp. 177 – 198, 2017.
- [41] A. Novellino, F. Cigna, M. Brahmi, A. Sowter, L. Bateson, and S. Marsh, "Assessing the feasibility of a national insar ground deformation map of great britain with sentinel-1," *Geosciences*, vol. 7, no. 2, 2017.
- [42] "European ground motion service (eu-gms) – a proposed copernicus service element," September 2017, <https://land.copernicus.eu/user-corner/technical-library/egms-white-paper>.